Materials Advances

PAPER

Cite this: *Mater. Adv.*, 2022, 3, 5786

Mixed dimensionality of 2D/3D heterojunctions for improving charge transport and long-term stability in high-efficiency 1.63 eV bandgap perovskite solar cells†

Jinkun Jiang, Congcong Tian, Zhiang Zhang, Xiao (Xiao) Liu, Xin Wang, Yiting Zheng, Zhanfei Zhang, Luyao Wang, Xueyun Wu, Jianghu Liang and Chun-Chao Chen *

Received 7th April 2022,
Accepted 23rd May 2022

DOI: 10.1039/d2ma00391k

rsc.li/materials-advances

Developing 2D/3D heterojunctions on 3D perovskite surfaces is an attractive strategy to improve the photovoltaic efficiency and stability of perovskite solar cells (PSCs). Particularly, the mixed dimensionality (MD) of 2D phases is found to be beneficial to both interfacial charge transport and device stability. Nevertheless, the control of dimensionality in aromatic spacers for 2D perovskites is very difficult. In addition to that, the use of 2D/3D heterojunctions on wider (~1.63 eV) bandgap perovskite solar cells is also uncommon. In this work, halogen *para*-substituted aromatic ligands based on R-α-methylbenzylammonium (R-α-MBA) were employed to form 2D capping layers on top of the wide-bandgap perovskite surface. The MD of the aromatic 2D capping layers (n = 1 and n = 2) was achieved through *para*-substitution with bromine (R-α-BrMBA), which increases the formation energy of the n = 1 phase. Thus, the interfacial charge transport was improved with the MD heterojunctions that had Type I band alignment, resulting in reduced energy loss. Furthermore, the introduction of aromatic ligands also flattens the surface morphologies and reduces the trap density. As a result, a champion power conversion efficiency (PCE) of 21.48% was delivered with an ultrahigh FF of 82.44% for 1.63 eV bandgap PSCs. Besides, long-term storage and thermal stabilities of the unencapsulated PSCs modified with R-α-BrMBA are substantially enhanced owing to the increased surface hydrophobicity and thermally stable MD passivation layers.

1. Introduction

Perovskite materials have become one of the most vital candidates in the photovoltaic field due to their excellent photoelectric properties, such as low exciton binding energy, long carrier lifetime and diffusion length, tunable band gap and high defect tolerance.[1–3] The past decade has witnessed a leap in the PCEs of organic–inorganic hybrid perovskite solar cells (OIHPSCs): from 3.8% first published in 2009 to 25.7% certified recently, surpassing the widely marketed polycrystalline silicon solar cells.[4] However, the PCE of single-junction PSCs still possesses tremendous space for improvement compared with the Shockley–Queisser (SQ) limit of 33.7%. Tandem solar cells based on wide-bandgap perovskites (bandgap >1.63 eV) are expected to be able to overcome the SQ limit and achieve higher PCEs in the future.[5–9] Thus, it is important to continuously improve the performance of wider bandgap (~1.63 eV) perovskite solar cells.

At present, the interface problem is the main factor affecting the PCE and stability of PSCs, including wide-bandgap PSCs, prepared by a low-temperature solution method.[10–14] Numerous defects such as dangling bonds, ion vacancies and grain boundaries (GBs) exist on the surface of the active layers due to the intrinsic ionic characteristics and polycrystalline properties of perovskites prepared by a solution method. These defect states eventually become the charge carrier capture centers, ion migration channels and the infiltration locations of water/oxygen, which can compromise the performance and stability of the devices. In order to optimize the device interfaces, surface modification strategies are commonly utilized to solve the interfacial problem.[15–18] Among them, modifying the surface of three-dimensional (3D) perovskite absorbers with two-dimensional (2D) Ruddlesden–Popper layered perovskites to form a 2D/3D heterojunction has attracted extensive attention in recent years. 2D perovskites possess higher environmental

---

School of Materials Science and Engineering, Shanghai Jiao Tong University, Shanghai 200240, P. R. China. E-mail: c3chen@sjtu.edu.cn

† Electronic supplementary information (ESI) available. See DOI: https://doi.org/10.1039/d2ma00391k

stability than their 3D counterparts due to the introduction of hydrophobic organic spacer cations in their crystal structure.[19] Besides, 2D perovskite capping layers do not only passivate the surface defects of 3D perovskite films, but also optimize the energy level arrangement at the perovskite/charge transport layer interface, which is conducive to improving the photovoltaic performance of PSCs.[20] Furthermore, a 2D perovskite with larger n is preferential to grow vertically, which is beneficial to charge transfer.[21] Thus, the dimensional regulation of 2D perovskite capping layers *via* their n-values is necessary to balance the PCE and stability.[22–25] He *et al.* introduced isopentylammonium iodide (PNAI) to develop multiple n-value 2D capping layers by tuning the post-treatment temperature, which optimized the charge transfer performance and decreased the interfacial voltage loss.[26] Yang *et al.* employed n-butylammonium bromide (BABr) to prepare stable and low-photovoltage-loss PSCs by covering bulk perovskites with mixed-dimensional 2D perovskite layers.[27] Azmi *et al.* tailored the dimensionality of the interfacial 2D-perovskite fragments with $n = 1$ and $n = 2$ phases by applying oleylammonium-iodide (OLAI), which enables efficient top-contact passivation through 2D-perovskite passivation layers.[28] However, it is evident that the dimensional regulation is more accessible for the 2D capping layers formed with alkyl ammonium spacers.

It was reported that the most widely used aromatic spacer ligand phenethylammonium (PEA) is not as functional as it should be on wide-bandgap PSCs and is more effective when it doesn't form 2D passivation layers.[13,15,29] Because of this, the control of dimensionality in 2D capping layers formed with aromatic ammonium spacers remains a difficult task. R-α-MBA is mainly adopted to prepare chiral 2D perovskites with unique spin-dependent properties, which have potential for use in advanced optical and spintronic devices.[30–33] For example, Kim *et al.* demonstrated a spin-polarized light-emitting diode (spin-LED) *via* chiral 2D perovskite $(\text{R-}\alpha\text{-MBA})_2\text{PbI}_4$.[34] Besides, Xu *et al.* introduced prepared $(\text{R-}\alpha\text{-ClMBA})_2\text{PbI}_4$, in which R-α-ClMBA is the chlorine-substituted analogue of R-α-MBA, into the 3D bulk perovskite recently.[35] They found that the 2D perovskite additive promoted more effective charge separation and achieved 21.78% PCE compared with 18.28% PCE of the control. In fact, the great potential of the aromatic spacers for 2D perovskites capped on 3D perovskites is waiting to be explored, particularly for wide-bandgap PSCs.

Herein, we developed 2D/3D heterojunctions on top of 3D wide-bandgap perovskites *via* halogen *para*-substituted aromatic cations based on R-α-MBA. Since the properties of aromatic spacers can be tuned by replacing hydrogen atoms on the benzene ring with functional groups to influence the crystal structures and electronic properties of 2D perovskites, the MD of 2D capping layers ($n = 1$ and $n = 2$) prepared from aromatic spacers was successfully achieved through *para*-substitution with bromine (Br) owing to the higher formation energy of the $n = 1$ phase for 2D perovskites. The aromatic 2D capping layer further displayed the capability to smooth the perovskite surface with less defect density compared to that of the control film. Correspondingly, the MD heterojunctions with Type I band alignment improve the interfacial charge transport and reduce the energy loss. As a result, we realized a champion PCE of 21.48% with an ultrahigh fill factor (*FF*) of 82.44%, which is among the best results for 1.63 eV bandgap perovskite solar cells. In addition, shielding of water/oxygen with thermally stable MD layers was also demonstrated, which is beneficial to long-term storage and thermal stabilities.

2. Results and discussion

In this work, aromatic cation R-α-methylbenzylammonium (R-α-MBA) and its halogen-substituted analogues of chloride salts (R-α-methyl-4-fluorobenzylammonium (R-α-FMBA), R-α-methyl-4-chlorobenzylammonium (R-α-ClMBA) and R-α-methyl-4-bromobenzylammonium (R-α-BrMBA)) (Fig. 1a) were adopted to form 2D perovskite layers on the surface of 3D films. The 2D/3D device structure is shown as Fig. 1b, in which the 3D wide-bandgap perovskite system is $\text{Rb}_{0.05}\text{Cs}_{0.05}(\text{FAPbI}_3)_{0.83}(\text{MAPbBr}_3)_{0.17}$ (bandgap = 1.63 eV) prepared from a one-step anti-solvent method, following our previous reports.[36,37]

In order to investigate the crystal structure of different 2D capping layers on 3D perovskites, X-ray diffraction (XRD) was carried out. As shown in Fig. 1c, all perovskite films present characteristic peaks of 3D perovskite at $2\theta = 14.2^\circ$, 28.5° and 31.9°, corresponding to the (110), (220) and (310) crystal planes of perovskite crystals, respectively.[38] In addition, new characteristic peaks appear at around $2\theta = 5.7^\circ$ for the perovskite films after surface modification, indicating the growth of 2D perovskites layers. To further understand the crystal structure of different 2D perovskites, the XRD patterns of $(\text{R-}\alpha\text{-MBA})_2\text{PbI}_2\text{Cl}_2$, $(\text{R-}\alpha\text{-MBA})_2\text{PbI}_2\text{Cl}_2$, $(\text{R-}\alpha\text{-MBA})_2\text{PbI}_2\text{Cl}_2$ and $(\text{R-}\alpha\text{-MBA})_2\text{PbI}_2\text{Cl}_2$ (2D films prepared by PbI_2 and the chloride salts) were demonstrated in Fig. 1d. Apparently, the 2D perovskites incorporated with halogen-substituted ligands present evenly spaced peaks from $2\theta = 5^\circ$ to $2\theta = 40^\circ$, which are ascribed to the crystallographic planes of (002), (004), (006), (008) and (0010). However, the diffraction peaks of the 2D perovskite incorporated with R-α-MBA (no halogen-substitution) is not spaced evenly. The more regular positions of the XRD peaks for 2D perovskites incorporated with halogen-substituted ligands imply that halogen atoms on the spacer ligands could improve the crystal orientation of the 2D perovskite phases due to hydrogen bonds between the halogen atoms and the hydrogen in adjacent benzene rings.[39] Besides, the peak positions and intensities of the XRD spectra for 2D perovskites incorporated with halogen-substituted ligands are slightly varied, which could be derived from the different distortions within the 2D perovskites induced by different functional halogen atoms and thus play a variational impact on film surface states.[40]

A scanning electron microscope (SEM) and atomic force microscope (AFM) were utilized to meticulously reveal the changes in the perovskite films surface with different modification. Fig. S1 (ESI†) manifests that the films modified with R-α-MBA and R-α-FMBA present uneven morphologies. After modified with R-α-ClMBA and R-α-BrMBA, the surface morphology

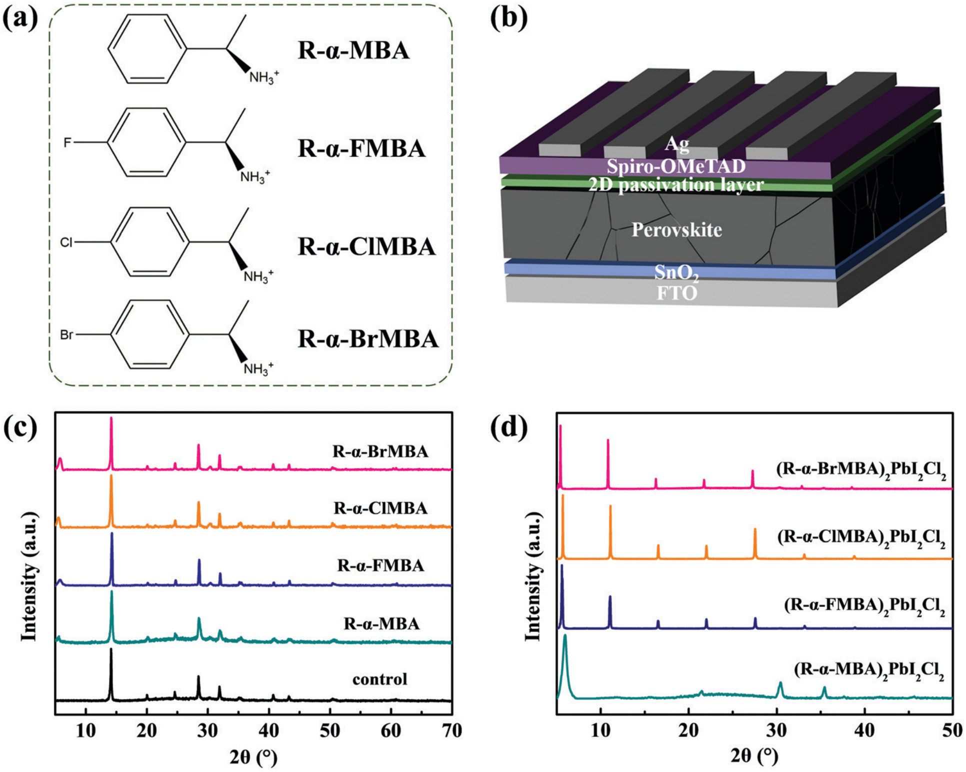

Fig. 1 (a) Chemical structure of R-α-MBA and halogen *para*-substituted aromatic ligands. (b) Schematic diagram of device structure. XRD patterns of (c) perovskite films modified with different organic ligands and (d) 2D perovskites with different ligands.

turned to be more uniform. This phenomenon could be ascribed to the different activation energies required for the interfacial reactions between halogen-substituted ligands and PbI_2.[41,42] Moreover, the root-mean-square (RMS) roughness decreases from 24.7 nm for the control film to 23.6 nm, 18.9 nm, 18.6 nm and 17.1 nm for the perovskite films modified with R-α-MBA, R-α-FMBA, R-α-ClMBA, and R-α-BrMBA, respectively. In other words, the surface of the perovskite/R-α-BrMBA film is the smoothest among all samples (Fig. S2, ESI†). It was reported that the transformation of the 3D perovskite to layered perovskite is progressive, and a slow transformation rate is much better for the quality and thickness control of 2D layers.[43] Therefore, the variation in the film roughness is possibly related to the different dimensional reduction process. The improved flatness of the perovskite film surface can benefit the close contact between the absorber and Spiro-OMeTAD, which can facilitate carrier transfer and inhibit non-radiative recombination at the perovskite/hole transport layer (HTL) interface.[44]

To further assess the effect of different treatments on perovskite films, steady-state photoluminescence (PL) and time-resolved photoluminescence (TRPL) measurements were implemented. As shown in Fig. 2a, PL peaks at 760 nm ascribed to bulk perovskites for 2D/3D films is significantly higher than that of the control film, indicating effectively reduced surface defects.[45] In particular, the strongest PL intensity for the perovskite/R-α-BrMBA film demonstrates the optimal passivation effect of the Br-2D perovskite. Besides, the PL peaks at 495 nm for the modified films illustrate the formation of 2D perovskites (n = 1).[46,47] Interestingly, the PL spectrum for the perovskite/R-α-BrMBA film presents another peak at 545 nm as shown in the inset of Fig. 2a, suggesting that the mixed dimensionality of n = 1 and n = 2 phases are formed for the Br-2D perovskite capping layer.[48] The optimized dimensional structure is beneficial for charge transport and transfer.[19] The TRPL decay curves for 2D/3D films are pictured in Fig. S3, (ESI†) and are fitted by a bi-exponential decay function: $f(t) = A_1\exp((-t)/\tau_1) + A_2\exp((-t)/\tau_2)$, where A_1 and A_2 are the corresponding decay amplitudes, τ_1 is the fast decay lifetime and related to the bimolecular recombination of photo-generated carriers, τ_2 is the slow decay lifetime and related to radiation recombination.[49,50] The corresponding fitted lifetime parameters are summarized in Table S1, (ESI†) among which τ_{avg} is the average carrier lifetime: $\tau_{avg} = ((A_1\tau_1^2+A_2\tau_2^2))/((A_1\tau_1 + A_2\tau_2))$.[51] The τ_{avg} is 221.90 ns, 305.38 ns, 315.03 ns, 470.41 ns and 541.33 ns for the control, R-α-MBA-, R-α-FMBA-, R-α-ClMBA-, and R-α-BrMBA-modified films, respectively, indicating the prolonged charge carrier lifetime due to surface modification with covered 2D perovskites. Furthermore, the longest τ_{avg} for the R-α-BrMBA-modified film confirms the effective suppression of the surface trap states and inhibition of the non-radiative recombination, which is consistent with the above PL results.

Furthermore, transient absorption (TA) spectra were measured to study the perovskite films with and without modification. It is found that only the perovskite film modified with

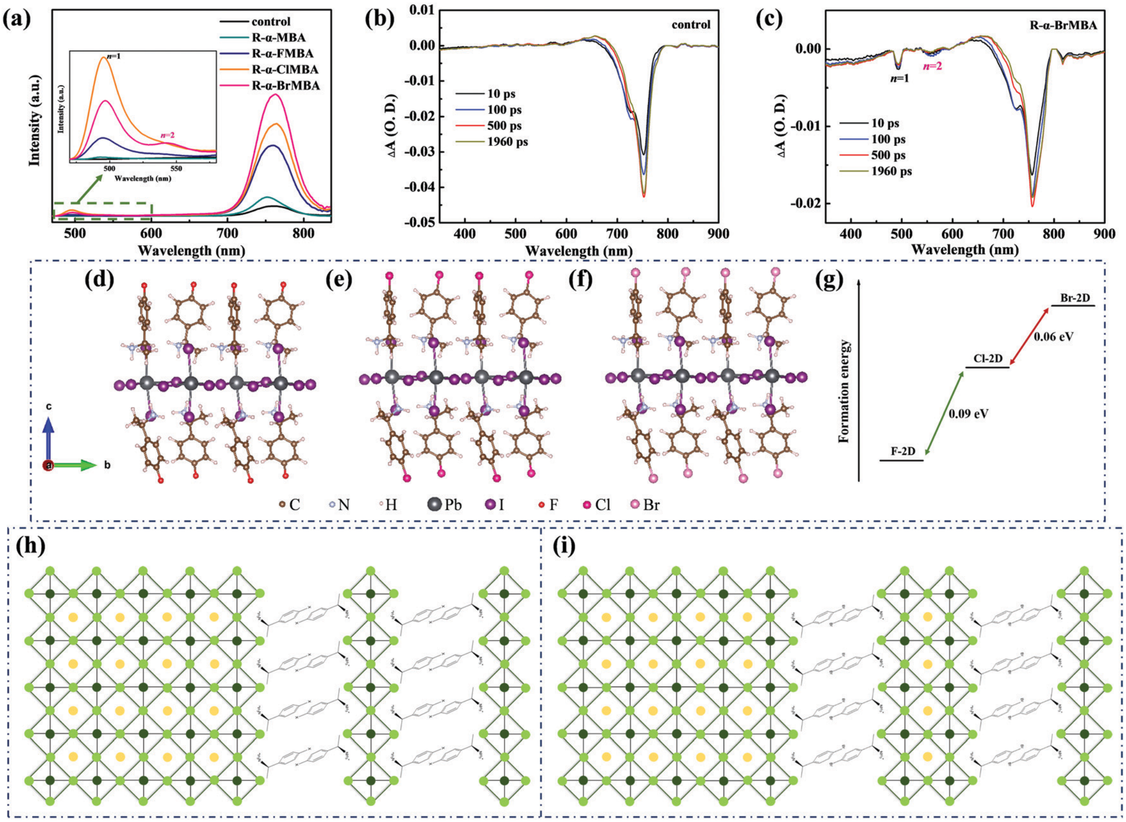

Fig. 2 (a) PL spectra of perovskite films modified with different organic ligands. TA spectra for the (b) control and (c) R-α-BrMBA-modified perovskite films. Optimized atomic models of different 2D perovskites (*n* = 1) (d) F-2D, (e) Cl-2D and (f) Br-2D by DFT calculations. (g) The relative formation energy difference between different 2D perovskites (*n* = 1). Structural diagrams of 2D perovskites on the surfaces modified with (h) R-α-XMBA (X = -F, -Cl) and (i) R-α-BrMBA.

R-α-BrMBA exhibits another two bleaching signals at 495 nm and 545 nm compared with the other films, which is assigned to the n = 1 and n = 2 phases of the 2D perovskite, respectively (Fig. 2b, c and Fig. S4, ESI†).[52] Furthermore, it was reported that the bulky molecules penetrate and slice the 3D perovskite lattice to develop 2D perovskite onto the surface *via* forming discrete multilayer Pb–I slabs and then thinning down the Pb–I slabs.[21,43,53] Therefore, the growth tendency of the 2D phases is closely related to their formation energy.[28] Based on this, first principles density functional theory (DFT) calculations were implemented to calculate the formation energy of F-2D, Cl-2D and Br-2D perovskites (n = 1) to disclose the mechanism of the dimensional change under different modification (Fig. 2d–f). We found that the formation energy of the Br-2D perovskite (n = 1) is higher than that of F-2D and Cl-2D perovskites (n = 1), suggesting that R-α-BrMBA is more prone to form higher-n phases (Fig. 2g).[43,54] Fig. S5 (ESI†) presents the calculated electrostatic surface potential (ESP) of R-α-FMBA, R-α-ClMBA and R-α-BrMBA molecules. The positive potential of the ammoniums gradually increases with the intensified electronegativity of bromine (Br), chlorine (Cl) and fluorine (F) atoms. Therefore, the activation energy required for reaction between R-α-BrMBA and perovskite is higher than that required for R-α-FMBA.[55,56] This means that the formation rate of the 2D layered perovskite with R-α-BrMBA is slower, which leads to uniformly covered film morphology. As a result, the regulated dimensionality is achieved by substituting different halogen atoms in our case.

Structural diagrams of 2D perovskites formed *via* the reaction between the 3D perovskite and R-α-XMBA (X = −F, −Cl, −Br) are portrayed according to the above analyses. The 2D perovskites formed with R-α-XMBA (X = −F, −Cl) modification only possess the phase of n = 1 as shown in Fig. 2h. However, the 2D perovskites formed with R-α-BrMBA modification possess mixed phases of n = 1 and n = 2 as shown in Fig. 2i. The higher n-value 2D phases are more conducive to the charge transport process at the perovskite/HTL interface, which boosts the efficiency of the PSCs.

In order to elucidate the effect of MD phases on the charge dynamics at the perovskite/HTL interfaces, PL and TRPL spectra were measured on the perovskite films covered with Spiro-OMeTAD. Fig. 3a and Fig. S6a (ESI†) show that the PL quenching for the R-α-BrMBA-modified film is more obvious than that of the control, R-α-MBA-, R-α-FMBA- and R-α-ClMBA-modified film, indicating that the Br-2D perovskite promotes the charge transport and accelerates the carrier quenching. The TRPL decay spectra are shown in Fig. 3b and Fig. S6b (ESI†). The corresponding fitted parameters are listed in Table S2 (ESI†). The faster quenching lifetime of the R-α-BrMBA-modified film

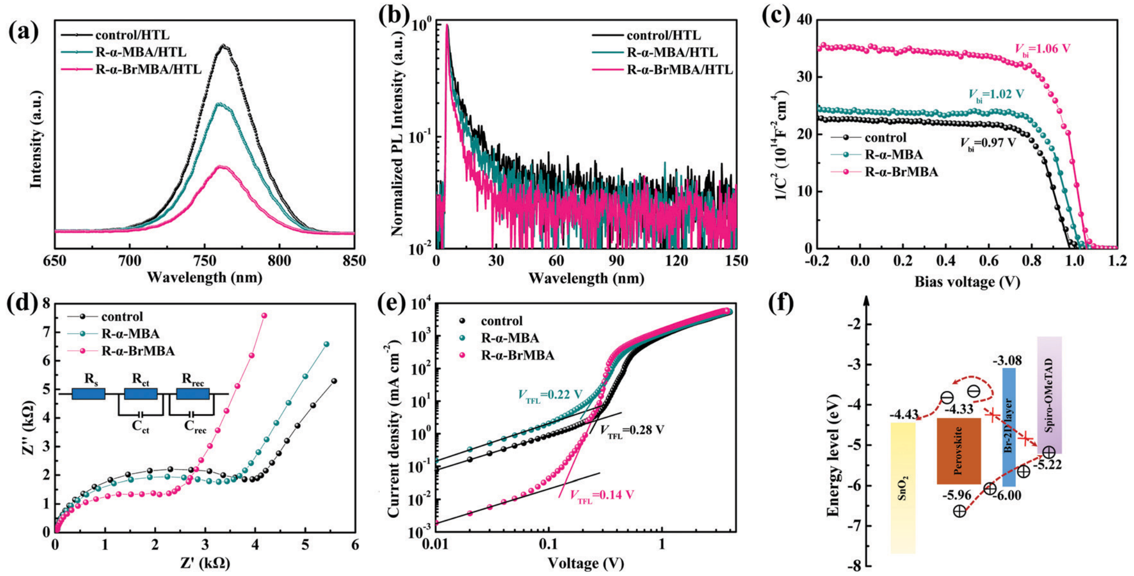

Fig. 3 (a) Steady-state PL spectra and (b) TRPL spectra of perovskite/HTL films with and without modification. (c) Mott–Schottky curves for different perovskite devices. (d) Nyquist plots of different perovskite devices. The dots and solid lines in (d) are the test data and fitted data, respectively. (e) SCLC curves for different perovskite devices. (f) Schematic illustration of energy level alignment.

compared with the other films suggests improved hole transfer from the perovskite to the Spiro-OMeTAD, which is consistent with the PL results.

We then investigated Mott–Schottky (M–S) analyses of the perovskite films with different modification. As shown in Fig. 3c and Fig. S7, (ESI†) the built-in voltage (V_{bi}) increases from 0.97 V of the control perovskite film to 1.06 V of the R-α-BrMBA-modified perovskite device. The enhanced V_{bi} may well extract hole carriers and repel electron carriers, reducing charge transfer loss and preventing surface recombination.[49] Therefore, the R-α-BrMBA-modified perovskite device with MD phases presents a more effective charge transfer, which is consistent with the PL and TRPL results.

Electrochemical impedance spectroscopy (EIS) was taken to further explore the charge transfer and recombination behavior for the devices. Nyquist plots of devices with different modification are shown in Fig. 3d and Fig. S8, (ESI†) and the inset in Fig. 3d displays the relevant equivalent circuit model. The left and right semicircles are corresponding to the charge transfer resistance (R_{ct}) and the recombination resistance (R_{rec}), respectively. It is can be seen that the R_{ct} decreases and the R_{rec} increases significantly after the devices are capped with 2D passivation layers (Table S3, ESI†). Moreover, the variation of the resistances for the R-α-BrMBA-modified PSC is more obvious than that of the other devices, indicating that MD phases can efficiently enhance the charge transfer and suppress the charge recombination at the interface.[50]

In addition, we prepared electron-only devices (FTO/SnO$_2$/3D perovskite/2D passivation layer/PCBM/Ag, as depicted in Fig. S9, ESI†) to measure the space charge limited current (SCLC) curves under dark conditions, as shown in Fig. 3e and Fig. S10 (ESI†). The charge mobility (μ) of the devices can be extracted from the SCLC curves following the equation: $\mu = (8L^3J)/(9\varepsilon_0\varepsilon_rV^2)$, where L, J, ε_0, ε_r, and V are the bulk perovskite thickness, current density, vacuum dielectric constant, relative dielectric constant of perovskite, and applied voltage, respectively.[57] The calculated μ increases from 1.38×10^{-2} cm^2 V^{-1} s^{-1} (control) to 1.97×10^{-2} cm^2 V^{-1} s^{-1} (R-α-BrMBA), as listed in Table S4 (ESI†). The highest μ for the R-α-BrMBA-modified device demonstrates that the interfacial MD phases well facilitate the charge transport at the perovskite/HTL interface, which is consistent with the above analyses. Furthermore, we quantitatively estimate the trap density of the devices *via* the equation: $N_t = (2\varepsilon_0\varepsilon_rV_{TFL})/(eL^2)$, where V_{TFL} is the trap-filled limit voltage.[58] As shown in Table S4, (ESI†) the optimal device based on R-α-BrMBA displays the lowest trap density of 4.22×10^{15} cm^{-3}, demonstrating that the passivation effect of R-α-BrMBA is much better than the others.

To further accurately explore the surface structure and chemical state of the perovskite film modified with R-α-BrMBA because of its preferable treatment effect, ultraviolet photoelectron spectroscopy (UPS) and X-ray photoelectron spectroscopy (XPS) were carried out. Fig. S11 (ESI†) suggests that the secondary electron cut-off edge and valence band edge for the 3D perovskite film are 16.56 eV and 1.30 eV, respectively, and those for the Br-2D/3D perovskite film are 16.54 eV and 1.32 eV, respectively. Based on the bandgaps (E_g) obtained from the ultraviolet-visible (UV-vis) absorption spectra and Tauc plots (Fig. S12, ESI†), Type I energy level alignment is depicted in Fig. 3f.[26,59] The energy level diagram signifies that the Br-2D perovskite is able to inhibit the transportation of electrons into Spiro-OMeTAD and reduce the electron–hole recombination probability efficiently.[53,60]

The XPS spectra are displayed in Fig. S13 (ESI†). The C 1s peaks of the control film at 284.8 eV and 286.3 eV are assigned to the C–C and C–NH$_2$ bonds, respectively, which are derived from the FA^+ and MA^+ of the perovskite. In addition, the C 1s peak at 288.1 eV is ascribed to the C═O bond caused by water/oxygen, as exhibited in Fig. S13a (ESI†). As for the Br-2D/3D perovskite film, the obviously increased C–NH_2 peak intensity in Fig. S13b (ESI†) demonstrates the existence of R-α-BrMBA on the surface. More importantly, the intensity of the C═O peak decreased dramatically, which indicates that the Br-2D perovskite capping layer is able to suppress the degradation of the absorber layer efficiently.[15,61] Fig. S13c and d (ESI†) reveal that the intensity of the N 1s peak at 401.8 eV assigned to the C–NH_2 bond increased obviously with the R-α-BrMBA modification, implying the existence of Br-2D perovskites.[61] Furthermore, the introduction of R-α-BrMBA is demonstrated by Fig. S13e (ESI†). Compared with the control perovskite film, the peaks from Pb 4f are shifted to lower binding energies and the peaks from Pb^0 are diminished in the perovskite film modified with R-α-BrMBA (Fig. S13f, ESI†), suggesting that the perovskite surface can be certainly passivated by R-α-BrMBA.[62]

Based on the above analyses, we can conclude that the R-α-BrMBA-modified device with MD phases possesses enhanced charge transport and suppressed non-radiative recombination at the perovskite/HTL interfaces compared with other devices. Next, we fabricated PSCs with a normal structure of FTO/SnO_2/3D perovskite/2D perovskite/Spiro-OMeTAD/Ag. Fig. S14 (ESI†) shows the cross-sectional SEM images of these devices. The current density–voltage (*J*–*V*) curves for PSCs modified with different concentrations of R-α-BrMBA are depicted in Fig. S15 (ESI†) and the corresponding photovoltaic parameters are listed in Table S5 (ESI†). The control device delivers a PCE of 18.97% with an open-circuit voltage (V_{OC}) of 1.12 V, a short-circuit current density (J_{SC}) of 21.60 mA cm^{-2}, and a fill factor (*FF*) of 78.41%. The PCEs of the PSCs first increased and then decreased with the addition of the R-α-BrMBA at different concentrations. This is because the covering of 2D phases is imperfect at low concentration, whereas the 2D layers are too thick to impair charge extraction at high concentrations, dramatically reducing the V_{OC} and *FF*. The device achieves a champion PCE of 21.48% with a V_{OC} of 1.20 V, a J_{SC} of 21.71 mA cm^{-2}, and a *FF* of 82.44% at a concentration of 4 mg mL^{-1} R-α-BrMBA. Besides, the PCE of 21.48% for PSCs modified with R-α-BrMBA is the highest compared with the PCEs of 20.32% and 20.87% for PSCs modified with R-α-FMBA and R-α-ClMBA, respectively, as shown in Fig. S16 and Table S6 (ESI†). The great improvement in PCEs of R-α-BrMBA-modified devices mainly originates from the increasing V_{OC} and *FF*, which could be attributed to the suppressed non-radiative recombination and enhanced charge transport.

Based on previous discussions, the excellent performance of R-α-BrMBA-modified devices was further compared with the control and R-α-MBA-modified devices as below. As shown in the *J*–*V* characteristics of the devices in Fig. 4a, the hysteresis index (HI) of the control, R-α-MBA-modified, and R-α-BrMBA-modified PSCs was calculated according to the equation:[63] HI = $((PCE_{reverse} - PCE_{forward}))/PCE_{reverse}$. The HI of R-α-BrMBA-modified PSCs is 3.07%, which is below the HI of 6.01% for the control PSCs and 4.69% for the R-α-MBA-modified PSCs (Table 1). The significantly reduced HI benefits from the more effective charge transport process and less trap density at the 3D/Br-2D/Spiro-OMeTAD interfaces as discussed previously. External quantum efficiency (EQE) spectra of the champion

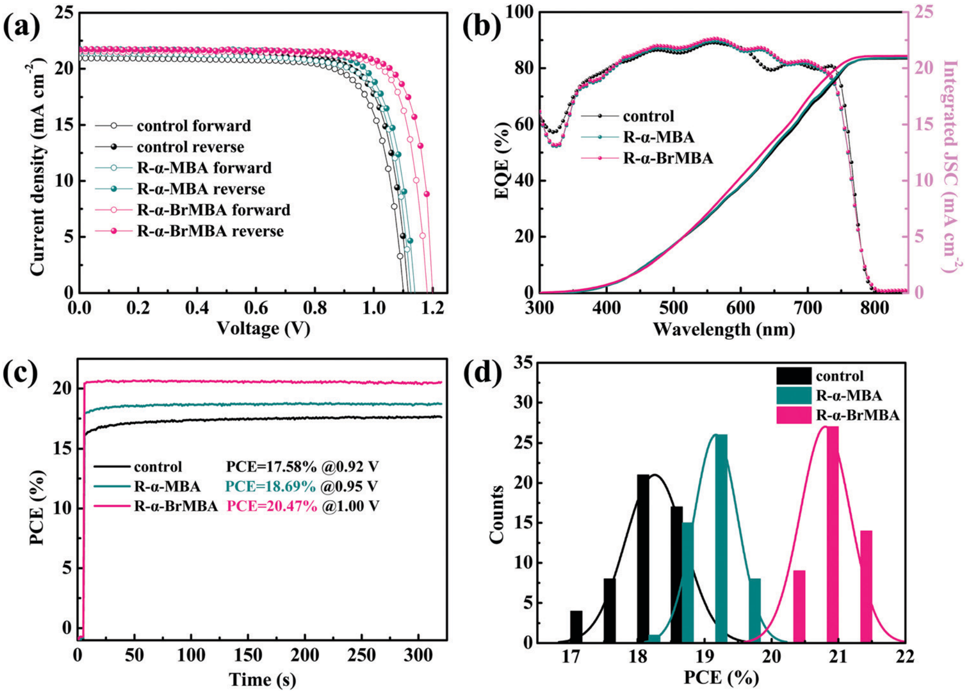

Fig. 4 Perovskite devices with different modifications. (a) *J*–*V* curves under forward and reverse scan, (b) EQE spectra, (c) steady-state output efficiency and (d) statistical distribution of PCEs.

Table 1 Photovoltaic parameters for PSCs under forward and reverse scanning

Samples	Directions	V_{OC} (V)	J_{sc} (mA cm^{-2})	FF (%)	PCE (%)	HI (%)
Control	Reverse	1.12	21.60	78.41	18.97	6.01
	Forward	1.10	20.87	77.68	17.83	
R-α-MBA	Reverse	1.14	21.65	79.47	19.61	4.69
	Forward	1.12	21.39	78.01	18.69	
R-α-BrMBA	Reverse	1.20	21.71	82.44	21.48	3.07
	Forward	1.18	21.59	81.73	20.82	

PSCs are depicted in Fig. 4b. The integrated J_{SC} values of the control, R-α-MBA- and R-α-BrMBA-modified devices are 20.89, 21.02 and 21.12 mA cm^{-2}, respectively, which match well with the values obtained from the measured *J–V* curves. The steady-state PCEs and current density were measured at the maximum power point of the PSCs, as shown in Fig. 4c and Fig. S17 (ESI†). A stabilized PCE of 20.47% and a stabilized J_{SC} of 20.76 mA cm^{-2} were obtained for the PSCs modified with R-α-BrMBA, while those of the control/R-α-MBA-modified devices are 17.58%/18.69% and 19.85/20.45 mA cm^{-2}, respectively. The PCEs of 50 devices of each type were statistically analyzed to study the reproducibility, as shown in Fig. 4d. It could be observed that the PSCs modified with R-α-BrMBA possess the optimum photovoltaic performance and narrowest distribution. The improvement in the PCEs was mainly due to the increase in the V_{OC} and *FF*, derived from the optimized carrier dynamics and interfacial state.

Specifically, *FF* loss, which consists of non-radiative loss and charge transport loss, was further studied. The *FF* maximum (FF_{max}) without charge transport loss can be calculated according to the equation: $FF_{max} = ((\nu_{OC} - \ln(\nu_{OC} + 0.72)))/((\nu_{OC} + 1))$, where $\nu_{OC} = (qV_{OC})/nkT$.[64] The n is the ideal factor and is extracted from the dark *J–V* curves in Fig. S18 (ESI†).[65] As shown in Fig. S19, (ESI†) compared with the control PSC, the non-radiative loss and charge transport loss are certainly suppressed for the PSC modified with R-α-MBA. These losses are further suppressed after modification with R-α-BrMBA, especially for the charge transport loss. The computation results again confirm that the Br-2D perovskite capping layer does not only reduce the surface trap states density and suppress non-radiative recombination, but also facilitates the charge carrier transport efficiently, resulting in boosted V_{OC}, *FF* and PCE.

Device stability is another important factor for PSCs except for PCEs. The water contact angle of different films was determined in order to evaluate the water resistance of PSCs with and without modification, as shown in Fig. 5a. The water

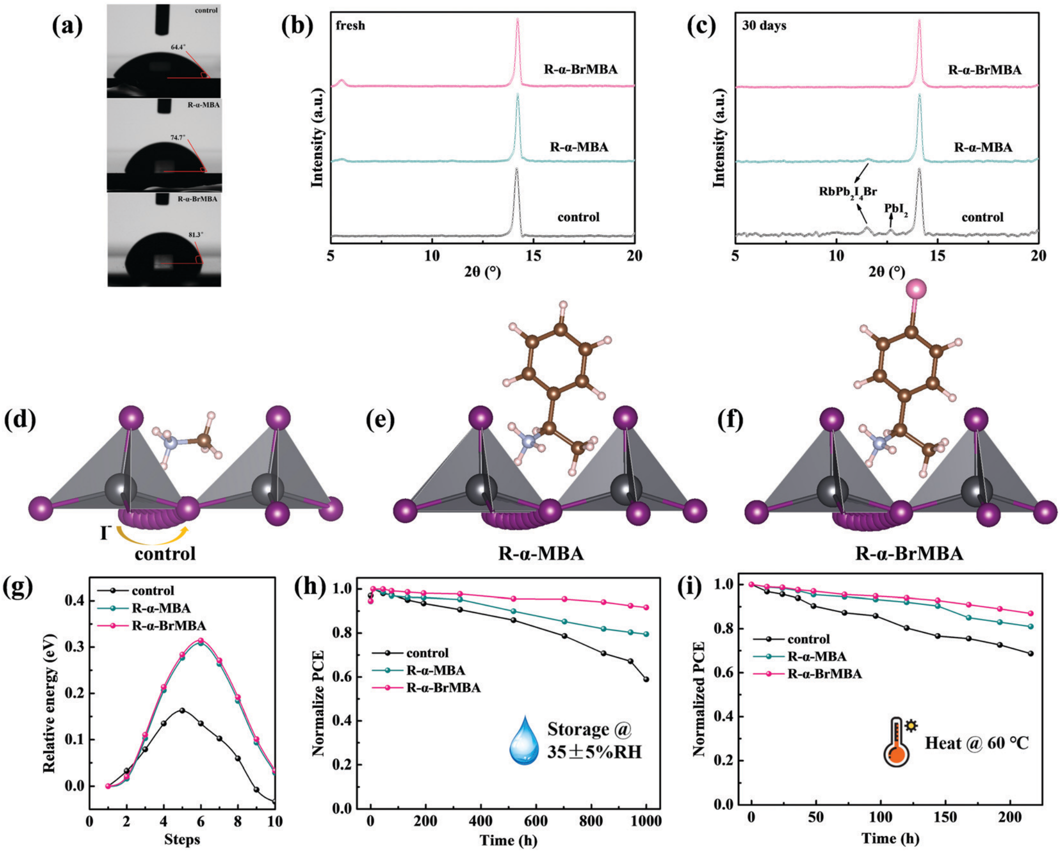

Fig. 5 (a) Water contact angle test of the perovskite films. XRD patterns of the perovskite films (b) fresh and (c) stored in a dry chamber (35 ± 5% RH and room temperature in the dark) for 30 days. I⁻ migration pathways as obtained from nudged elastic band (NEB) calculations for the perovskite films (d) control, (e) R-α-MBA-incorporated and (f) R-α-BrMBA-incorporated. (g) Ion migration energy of different modification. (h) Long-term storage stability test of unencapsulated PSCs. (i) Thermal stability test of unencapsulated PSCs annealed under a N_2 atmosphere.

contact angle of the control film is only 64.4°. Moreover, the water contact angle for the R-α-MBA-modified film is 74.7° and increases to 81.3° for the R-α-BrMBA-modified film, which may be due to the more homogeneous morphology and bromine atom. XRD patterns were obtained on the fresh films and the films stored in the dry chamber (35 ± 5% RH and room temperature in dark) for 30 days. As shown in Fig. 5c, the control film has two additional peaks at 11.4° and 12.7°, which are assigned to $RbPb_2I_4Br$ and PbI_2, respectively, after being aged for 30 days (Fig. 5b).[66] However, the degradation is certainly inhibited for the R-α-MBA- and R-α-BrMBA-modified films, which means that the I^- migration is suppressed.

In order to theoretically study the mechanism of the distinct phenomena, we performed DFT simulations to model the ion migration pathway at interfaces (Fig. 5c–e) and calculated the I^- migration energy between two I^- vacancies (Fig. 5f). We can find that the migration distances are extended for both R-α-MBA- and R-α-BrMBA-incorporated cases.[67] Furthermore, the calculated migration energy for R-α-MBA- and R-α-BrMBA-incorporated cases are around two-fold higher than that of the control.[68] The substantially higher migration energy indicates that I^- ion migration in the 2D/3D layers is suppressed significantly, which may be due to the steric impediment effect from larger spacer cations. Correspondingly, the unencapsulated PSCs modified with R-α-MBA and R-α-BrMBA maintained ∼80% and ∼90% of their initial PCEs after 1000 h of storage, respectively. Nevertheless, the control PSC only retained ∼58% of its initial PCE during the same period. In addition, the thermal stability of the MD heterojunction was investigated. The PL spectra of fresh and thermal aged perovskite films modified with R-α-BrMBA are shown in Fig. S20 (ESI†). The result implies that the dimensionality of the MD phases remains the same after annealing at 60 °C in N_2 for 8 days. We also conducted thermal stability testing of the devices, in which the Spiro-OMeTAD was replaced by PTAA. The PCE of R-α-MBA- and R-α-BrMBA-modified PSCs without encapsulation maintained 81% and ∼87% of their original values after 216 h of annealing in N_2, whereas the control PSC without encapsulation decreased to ∼68% of its initial PCEs under the same condition, respectively. The improved long-term storage and thermal stabilities of the R-α-BrMBA-modified PSC can be explained by the reduced trap density, suppressed ion migration and thermally robust MD heterojunction derived from the Br-2D passivation layers.

3. Conclusions

In summary, we employed R-α-MBA based halogen-substituted aromatic cations to prepare efficient and stable 2D/3D wide-bandgap PSCs. We found that the perovskite film modified with bromine-substituted aromatic ligand R-α-BrMBA presents the smoothest surface and the optimal passivation effect compared with the others, resulting in the reduction of the non-radiative loss. Besides, R-α-BrMBA induces MD in 2D phases on top of the bulk perovskite absorber layers, owing to its higher formation energy to develop the $n = 1$ phase for the 2D perovskite. Therefore, the charge transport behavior at the perovskite/HTL interface is optimized with Type I band alignment, leading to less energy loss. As a result, a champion PCE of 21.48% with an ultrahigh *FF* of 82.44% and an ultrahigh V_{OC} of 1.20 V is achieved for 1.63 eV perovskite solar cells. Moreover, the increased surface hydrophobicity, inhibited ion migration and thermally robust MD heterojunctions obviously enhanced the stabilities of Br-2D/3D wide-bandgap PSCs. Our findings provide a promising method to construct more effective 2D/3D heterojunctions by regulating the dimensionality of covered 2D perovskites formed with aromatic ligands, and achieve highly efficient wide-bandgap PSCs with simultaneously improved stability for future applications.

Author contributions

Jinkun Jiang: writing original draft, experiment and characterization, data analysis; Congcong Tian: synthesizing R-α-MBACl; Zhiang Zhang: data analysis, theoretical calculation, characterization; Xiao Liu: data analysis, characterization; Xin Wang: revising the draft; Yiting Zheng: data analysis, revising the draft; Zhanfei Zhang: revising the draft; Luyan Wang: experimental guidance; Xueyun Wu: characterization; Jianghu Liang: revising the draft; Chun-Chao Chen: supervision, revising the draft, project administration.

Conflicts of interest

There are no conflicts of interest to declare.

Acknowledgements

This study was funded by the Natural Science Foundation of Shanghai (22ZR1428200), the National Natural Science Foundation of China (Grant no. 51950410581), the Shanghai Government (20JC141500), and CATL–SJTU joint funding.

References

1 Y. Fu, H. Zhu, J. Chen, M. P. Hautzinger, X. Y. Zhu and S. Jin, *Nat. Rev. Mater.*, 2019, **4**, 169–188.
2 J. Huang, Y. Yuan, Y. Shao and Y. Yan, *Nat. Rev. Mater.*, 2017, **2**, 17042.
3 A. K. Jena, A. Kulkarni and T. Miyasaka, *Chem. Rev.*, 2019, **119**, 3036–3103.
4 Best-reserch-cell-efficiencies. **https://www.nrel.gov/pv/cell-efficiency.html**.
5 M. De Bastiani, A. J. Mirabelli, Y. Hou, F. Gota, E. Aydin, T. G. Allen, J. Troughton, A. S. Subbiah, F. H. Isikgor, J. Liu, L. Xu, B. Chen, E. Van Kerschaver, D. Baran, B. Fraboni, M. F. Salvador, U. W. Paetzold, E. H. Sargent and S. De Wolf, *Nat. Energy*, 2021, **6**, 167–175.

6 M. I. Hossain, A. M. Saleque, S. Ahmed, I. Saidjafarzoda, M. Shahiduzzaman, W. Qarony, D. Knipp, N. Biyikli and Y. H. Tsang, *Nano Energy*, 2021, **79**, 105400.

7 A. Al-Ashouri, E. Köhnen, B. Li, A. Magomedov, H. Hempel, P. Caprioglio, J. A. Márquez, A. B.-M. Vilches, E. Kasparavicius, J. A. Smith, N. Phung, D. Menzel, M. Grischek, L. Kegelmann, D. Skroblin, C. Gollwitzer, T. Malinauskas, M. Jošt, G. Matič, B. Rech, R. Schlatmann, M. Topič, L. Korte, A. Abate, B. Stannowski, D. Neher, M. Stolterfoht, T. Unold, V. Getautis and S. Albrecht, *Science*, 2020, **370**, 1300–1309.

8 K. Xiao, R. Lin, Q. Han, Y. Hou, Z. Qin, H. T. Nguyen, J. Wen, M. Wei, V. Yeddu, M. I. Saidaminov, Y. Gao, X. Luo, Y. Wang, H. Gao, C. Zhang, J. Xu, J. Zhu, E. H. Sargent and H. Tan, *Nat. Energy*, 2020, **5**, 870–880.

9 B. Chen, Z. J. Yu, S. Manzoor, S. Wang, W. Weigand, Z. Yu, G. Yang, Z. Ni, X. Dai, Z. C. Holman and J. Huang, *Joule*, 2020, **4**, 850–864.

10 J. Y. Kim, J. W. Lee, H. S. Jung, H. Shin and N. G. Park, *Chem. Rev.*, 2020, **120**, 7867–7918.

11 J.-P. Correa-Baena, W. Tress, K. Domanski, E. H. Anaraki, S.-H. Turren-Cruz, B. Roose, P. P. Boix, M. Grätzel, M. Saliba, A. Abate and A. Hagfeldt, *Energy Environ. Sci.*, 2017, **10**, 1207–1212.

12 Y. Zhou, F. Wang, Y. Cao, J.-P. Wang, H.-H. Fang, M. A. Loi, N. Zhao and C.-P. Wong, *Adv. Energy Mater.*, 2017, **7**, 1701048.

13 J. Zhuang, P. Mao, Y. Luan, X. Yi, Z. Tu, Y. Zhang, Y. Yi, Y. Wei, N. Chen, T. Lin, F. Wang, C. Li and J. Wang, *ACS Energy Lett.*, 2019, **4**, 2913–2921.

14 J. He, J. Liu, Y. Hou, Y. Wang, S. Yang and H. G. Yang, *Nat. Commun.*, 2020, **11**, 4237.

15 Q. Jiang, Y. Zhao, X. Zhang, X. Yang, Y. Chen, Z. Chu, Q. Ye, X. Li, Z. Yin and J. You, *Nat. Photonics*, 2019, **13**, 460–466.

16 Q. Song, H. Gong, C. Ji, H. Zhang, F. Sun, F. You, Z. He, D. Li and C. Liang, *Sol. RRL*, 2021, **5**, 2100472.

17 J. Suo, B. Yang, E. Mosconi, H. S. Choi, Y. Kim, S. M. Zakeeruddin, F. De Angelis, M. Grätzel, H. S. Kim and A. Hagfeldt, *Adv. Funct. Mater.*, 2021, **31**, 2102902.

18 E. Akman and S. Akin, *Adv. Mater.*, 2021, **33**, 2006087.

19 G. Grancini and M. K. Nazeeruddin, *Nat. Rev. Mater.*, 2018, **4**, 4–22.

20 P. Chen, Y. Bai, S. Wang, M. Lyu, J.-H. Yun and L. Wang, *Adv. Funct. Mater.*, 2018, **28**, 1706923.

21 R. Quintero-Bermudez, A. Gold-Parker, A. H. Proppe, R. Munir, Z. Yang, S. O. Kelley, A. Amassian, M. F. Toney and E. H. Sargent, *Nat. Mater.*, 2018, **17**, 900–907.

22 P. Gao, A. R. Bin Mohd Yusoff and M. K. Nazeeruddin, *Nat. Commun.*, 2018, **9**, 5028.

23 T. Bu, J. Li, Q. Lin, D. P. McMeekin, J. Sun, M. Wang, W. Chen, X. Wen, W. Mao, C. R. McNeill, W. Huang, X.-L. Zhang, J. Zhong, Y.-B. Cheng, U. Bach and F. Huang, *Nano Energy*, 2020, **75**, 104917.

24 Y. Lin, Y. Bai, Y. Fang, Z. Chen, S. Yang, X. Zheng, S. Tang, Y. Liu, J. Zhao and J. Huang, *J. Phys. Chem. Lett.*, 2018, **9**, 654–658.

25 H. Wang, C. Zhu, L. Liu, S. Ma, P. Liu, J. Wu, C. Shi, Q. Du, Y. Hao, S. Xiang, H. Chen, P. Chen, Y. Bai, H. Zhou, Y. Li and Q. Chen, *Adv. Mater.*, 2019, **31**, e1904408.

26 M. He, J. Liang, Z. Zhang, Y. Qiu, Z. Deng, H. Xu, J. Wang, Y. Yang, Z. Chen and C.-C. Chen, *J. Mater. Chem. A*, 2020, **8**, 25831–25841.

27 G. Yang, Z. Ren, K. Liu, M. Qin, W. Deng, H. Zhang, H. Wang, J. Liang, F. Ye, Q. Liang, H. Yin, Y. Chen, Y. Zhuang, S. Li, B. Gao, J. Wang, T. Shi, X. Wang, X. Lu, H. Wu, J. Hou, D. Lei, S. K. So, Y. Yang, G. Fang and G. Li, *Nat. Photonics*, 2021, **15**, 681–689.

28 R. Azmi, E. Ugur, A. Seitkhan, F. Aljamaan, A. S. Subbiah, J. Liu, G. T. Harrison, M. I. Nugraa, M. K. Eswaran, M. Babics, Y. Chen, F. Xu, T. G. Allen, A. U. Rehman, C.-L. Wang, T. D. Anthopoulos, U. Schwingenschlögl, M. D. Bastiani, E. Aydin and S. D. Wolf, *Science*, 2022, **376**, 73–77.

29 J. Wang, S. Fu, X. Liu, H. Yuan, Z. Xu, C. Wang, J. Zhang, L. Huang, Z. Hu and Y. Zhu, *J. Alloys Compd.*, 2021, **891**, 161971.

30 J. Ahn, E. Lee, J. Tan, W. Yang, B. Kim and J. Moon, *Mater. Horiz.*, 2017, **4**, 851–856.

31 G. Long, C. Jiang, R. Sabatini, Z. Yang, M. Wei, L. N. Quan, Q. Liang, A. Rasmita, M. Askerka, G. Walters, X. Gong, J. Xing, X. Wen, R. Quintero-Bermudez, H. Yuan, G. Xing, X. R. Wang, D. Song, O. Voznyy, M. Zhang, S. Hoogland, W. Gao, Q. Xiong and E. H. Sargent, *Nat. Photonics*, 2018, **12**, 528–533.

32 H. Lu, J. Wang, C. Xiao, X. Pan, X. Chen, R. Brunecky, J. J. Berry, K. Zhu, M. C. Beard and Z. V. Vardeny, *Sci. Adv.*, 2019, **5**, eaay0571.

33 J. Wang, H. Lu, X. Pan, J. Xu, H. Liu, X. Liu, D. R. Khanal, M. F. Toney, M. C. Beard and Z. V. Vardeny, *ACS Nano*, 2021, **15**, 588–595.

34 Y.-H. Kim, Y. Zhai, H. Lu, X. Pan, C. Xiao, E. A. Gaulding, S. P. Harvey, J. J. Berry, Z. V. Vardeny, J. M. Luther and M. C. Beard, *Science*, 2021, **371**, 1129–1133.

35 X. L. Xu, L. B. Xiao, J. Zhao, B. K. Pan, J. Li, W. Q. Liao, R. G. Xiong and G. F. Zou, *Angew. Chem., Int. Ed.*, 2020, **59**, 19974–19982.

36 X. Liu, Z. Zhang, J. Jiang, C. Tian, X. Wang, L. Wang, Z. Zhang, X. Wu, Y. Zheng, J. Liang and C.-C. Chen, *Chem. Eng. J.*, 2022, **432**, 134382.

37 Z. Zhang, J. Jiang, X. Xiao Liu, X. Wang, L. Wang, Y. Qiu, Z. Zhang, Y. Zheng, X. Wu, J. Liang, C. Tian and C. C. Chen, *Small*, 2022, **18**, e2105184.

38 S. Luo and W. A. Daoud, *Materials*, 2016, **9**, 123.

39 H. Pan, X. Zhao, X. Gong, Y. Shen and M. Wang, *J. Phys. Chem. Lett.*, 2019, **10**, 1813–1819.

40 B. Saparov and D. B. Mitzi, *Chem. Rev.*, 2016, **116**, 4558–4596.

41 J. Hu, I. W.-H. Ostwald, S. J. Stuard, M. M. Nahid, N. Zhou, O. F. Williams, Z. Guo, L. Yan, H. Hu, Z. Chen, X. Xiao, Y. Lin, Z. Yang, J. Huang, A. M. Moran, H. Ade, J. R. Neilson and W. You, *Nat. Commun.*, 2019, **10**, 1276.

42 S. Zhao, J. Xie, G. Cheng, Y. Xiang, H. Zhu, W. Guo, H. Wang, M. Qin, X. Lu, J. Qu, J. Wang, J. Xu and K. Yan, *Small*, 2018, **14**, e1803350.

43 A. H. Proppe, A. Johnston, S. Teale, A. Mahata, R. Quintero-Bermudez, E. H. Jung, L. Grater, T. Cui, T. Filleter,

C. Y. Kim, S. O. Kelley, F. De Angelis and E. H. Sargent, *Nat. Commun.*, 2021, **12**, 3472.

44 M. U. Rothmann, W. Li, J. Etheridge and Y. B. Cheng, *Adv. Energy Mater.*, 2017, **7**, 1700912.

45 L. Wang, X. Wang, L. Zhu, S.-B. Leng, J. Liang, Y. Zheng, Z. Zhang, Z. Zhang, X. Liu, F. Liu and C.-C. Chen, *Chem. Eng. J.*, 2022, **430**, 132730.

46 S. Zhang, L. Zhang, Q. Tian, X. Gu, Y. Du, K. Zhao and S. Liu, *Adv. Energy Mater.*, 2021, **12**, 2103007.

47 W. Li, X. Gu, C. Shan, X. Lai, X. W. Sun and A. K.-K. Kyaw, *Nano Energy*, 2022, **91**, 106666.

48 J. Liang, Z. Zhang, Q. Xue, Y. Zheng, X. Wu, Y. Huang, X. Wang, C. Qin, Z. Chen and C.-C. Chen, *Energy Environ. Sci.*, 2022, **15**, 296–310.

49 C. C. Zhang, Z. K. Wang, S. Yuan, R. Wang, M. Li, M. F. Jimoh, L. S. Liao and Y. Yang, *Adv. Mater.*, 2019, **31**, e1902222.

50 F. Wang, M. Yang, Y. Zhang, J. Du, S. Yang, L. Yang, L. Fan, Y. Sui, Y. Sun and J. Yang, *Nano Res.*, 2021, **14**, 2783–2789.

51 W. Zhao, J. Xu, K. He, Y. Cai, Y. Han, S. Yang, S. Zhan, D. Wang, Z. Liu and S. Liu, *Nanomicro Lett.*, 2021, **13**, 169.

52 M. E.-F. Bouduban, V. I.-E. Queloz, V. M. Caselli, K. T. Cho, A. R. Kirmani, S. Paek, C. Roldan-Carmona, L. J. Richter, J. E. Moser, T. J. Savenije, M. K. Nazeeruddin and G. Grancini, *J. Phys. Chem. Lett.*, 2019, **10**, 5713–5720.

53 Z. Liu, K. Meng, X. Wang, Z. Qiao, Q. Xu, S. Li, L. Cheng, Z. Li and G. Chen, *Nano Lett.*, 2020, **20**, 1296–1304.

54 J. Xing, Y. Zhao, M. Askerka, L. N. Quan, X. Gong, W. Zhao, J. Zhao, H. Tan, G. Long, L. Gao, Z. Yang, O. Voznyy, J. Tang, Z. H. Lu, Q. Xiong and E. H. Sargent, *Nat. Commun.*, 2018, **9**, 3541.

55 T. Wu, Y. Wang, X. Li, Y. Wu, X. Meng, D. Cui, X. Yang and L. Han, *Adv. Energy Mater.*, 2019, **9**, 1803766.

56 D. Xin, S. Tie, X. Zheng, J. Zhu and W.-H. Zhang, *J. Energy Chem.*, 2020, **46**, 173–177.

57 M. Nikolka, K. Broch, J. Armitage, D. Hanifi, P. J. Nowack, D. Venkateshvaran, A. Sadhanala, J. Saska, M. Mascal, S. H. Jung, J. K. Lee, I. McCulloch, A. Salleo and H. Sirringhaus, *Nat. Commun.*, 2019, **10**, 2122.

58 X. Wang, Y. Qiu, L. Wang, T. Zhang, L. Zhu, T. Shan, Y. Wang, J. Jiang, L. Kong, H. Zhong, H. Yu, F. Liu, F. Gao, F. Wang and C.-C. Chen, *Nano Energy*, 2021, **89**, 106445.

59 S. Paek, C. Roldan-Carmona, K. T. Cho, M. Franckevicius, H. Kim, H. Kanda, N. Drigo, K. H. Lin, M. Pei, R. Gegevicius, H. J. Yun, H. Yang, P. A. Schouwink, C. Corminboeuf, A. M. Asiri and M. K. Nazeeruddin, *Adv. Sci.*, 2020, **7**, 2001014.

60 Y.-W. Jang, S. Lee, K. M. Yeom, K. Jeong, K. Choi, M. Choi and J. H. Noh, *Nat. Energy*, 2021, **6**, 63–71.

61 G. Liu, H. Zheng, H. Xu, L. Zhang, X. Xu, S. Xu and X. Pan, *Nano Energy*, 2020, **73**, 104753.

62 Y. Du, J. Wu, X. Zhang, Q. Zhu, M. Zhang, X. Liu, Y. Zou, S. Wang and W. Sun, *J. Energy Chem.*, 2021, **52**, 84–91.

63 G. Kim, H. Min, K. S. Lee, D. Y. Lee, S. M. Yoon and S. I. Seok, *Science*, 2020, **370**, 108–112.

64 M. A. Green, *Sol. Cells*, 1982, **7**, 337–340.

65 T. He, S. Li, Y. Jiang, C. Qin, M. Cui, L. Qiao, H. Xu, J. Yang, R. Long, H. Wang and M. Yuan, *Nat. Commun.*, 2020, **11**, 1672.

66 Y. Hu, M. F. Aygüler, M. L. Petrus, T. Bein and P. Docampo, *ACS Energy Lett.*, 2017, **2**, 2212–2218.

67 J. Yang, W. Sheng, R. Li, L. Gong, Y. Li, L. Tan, Q. Lin and Y. Chen, *Adv. Energy Mater.*, 2022, 2103652.

68 S. Tan, I. Yavuz, N. De Marco, T. Huang, S. J. Lee, C. S. Choi, M. Wang, S. Nuryyeva, R. Wang, Y. Zhao, H. C. Wang, T. H. Han, B. Dunn, Y. Huang, J. W. Lee and Y. Yang, *Adv. Mater.*, 2020, **32**, e1906995.